

Mesoscopic fluctuations of off-diagonal matrix elements of the angular momentum and orbital magnetism of free electrons in a rectangular box.

M. X. Lou, J. M. A. S. P. Wickramasinghe and R. A. Serota

Department of Physics

University of Cincinnati

Cincinnati, OH 45221-0011

Abstract

We study, analytically and numerically, mesoscopic fluctuations of the off-diagonal matrix elements of the orbital angular momentum between the nearest energy levels $i = (n_x, n_y)$ and $f = (k_x, k_y)$ in a rectangular box with incommensurate sides. In the semiclassical regime, where the level number of i is $\mathcal{N} \gg 1$, our derivation gives $\left\langle \left| \hat{L}_{if} \right|^2 \right\rangle \sim \sqrt{\mathcal{N}}$. Numerical simulations, using simultaneous ensemble averaging (over the aspect ratios of rectangles) and spectral averaging (over the energy interval), are in excellent agreement with this analytical prediction. Physically, the mean is dominated by the level pairs $k_x = n_x \pm 1$, $k_y = n_y \mp 1$. Also in a rectangular box, we investigate the mean orbital susceptibility of a free electron gas and argue that it reduces, up to a coefficient, to the two-level van Vleck susceptibility that involves the last occupied (Fermi) level i and the first unoccupied level f . This result is confirmed numerically as well, albeit the effect of fluctuations is much more pronounced for the susceptibility since it is due both to large fluctuations in $\left\langle \left| \hat{L}_{if} \right|^2 \right\rangle$ and in level separations $\varepsilon_f - \varepsilon_i$ (level bunching).

I. OFF-DIAGONAL MATRIX ELEMENTS OF THE ANGULAR MOMENTUM

A. Introduction

Off-diagonal matrix elements of the orbital angular momentum enter into important physical quantities, such as magnetic dipole absorption and van Vleck susceptibility. This is particularly significant in the situations when the angular momentum is not a good quantum number. Such is the case in disordered systems where, in the semiclassical approximation, it was shown that in 2D

$$\left\langle \left| \hat{L}_{if} \right|^2 \right\rangle \sim \varepsilon_F \tau \sim k_F \ell \quad (1)$$

Here k_F is the wave number of a free particle whose energy ε_F corresponds to level i , and ℓ and τ are, respectively, the mean-free-path and the scattering time due to disorder. This result can be derived either by considering the classical magneto-dipole absorption [1], [2] or by a direct evaluation [1] using the technique developed in Refs. [3], [4].

Disordered systems are classically chaotic. In the semiclassical regime they exhibit "level rigidity," which prevents large fluctuations in the level spacings and, in turn, large fluctuations of the number of levels in an energy interval. [5]- [7] Classically integrable systems, on the other hand, exhibit "level bunching" characterized by large fluctuations in level spacings¹ and high occurrence of small spacings - hence the term - and, in turn, large fluctuations in the number of levels in an energy interval. [5], [6] (It was recently shown that such behavior extends only up to a certain energy scale, upon which strong correlations between levels set in [8]; Even then, the number level variance exhibit large, non-decaying oscillations around the "saturation value.") Consequently, the mesoscopic, or non self-averaging, effects are expected to be more pronounced in integrable systems.

¹In the absence of resonances, or supersymmetry, such as the case for harmonic oscillator and the Kepler problem.

The fluctuations in the level spacings (and more generally, the specifics of correlations between the levels) is, however, just one of the factors contributing to the mesoscopic fluctuations of physical quantities. Other contributors are expected to fluctuate much stronger in classically integrable systems than in classically chaotic systems as well. In the first part of this paper we consider the fluctuations of the off-diagonal matrix elements of the angular momentum in a rectangular box. We will show, in particular, that

$$\left\langle \left| \hat{L}_{if} \right|^2 \right\rangle \sim \sqrt{\mathcal{N}} \sim k_F L \quad (2)$$

where $\mathcal{N} \gg 1$ is the level number of i and L is a rectangle's side.

Brackets in eq. (1) denote averaging over various realizations of disorder, which is an example of "ensemble averaging." A natural extension of the concept of ensemble averaging to a rectangular box would be to average over the aspect ratios of the rectangles' sides. However, our analytical derivation of eq. (2) is based on "spectral averaging," that is averaging over an energy interval. A detailed explanation of our numerical procedure will be given in text, but it should be already mentioned that a *combined* ensemble and spectral averaging was performed. The former involves averaging over the aspect ratios chosen to be algebraic and close to 1. The latter is over an energy interval that includes a large number of pairs (i, f) and is, in fact, necessary due to large fluctuations in $\left| \hat{L}_{if} \right|^2$. In other words, spectral averaging proves essential both in order to derive a closed form analytical expression and to ensure convergence of numerical results. Clearly, an underlying assumption is the validity of the "ergodic hypothesis" - that the two averages are equivalent.

This Section is organized as follows. First, we show that the magnitude of $\left| \hat{L}_{if} \right|^2$ is determined by the hierarchy of (odd) pairs $(k_x - n_x)$ and $(k_y - n_y)$, where $i = (n_x, n_y)$ and $f = (k_x, k_y)$ are the nearest energy levels. For a given pair, $\left| \hat{L}_{if} \right|^2 \propto \mathcal{N}$ with the largest coefficient, by two orders of magnitude, corresponding to $k_x = n_x \pm 1, k_y = n_y \mp 1$. Moreover, we show that the probability of the latter $\propto \mathcal{N}^{-1/2}$, while for most pairs it is $\propto \mathcal{N}^{-1}$. Consequently, such pairs give an overwhelming contribution to the spectral average, which results in eq. (2). This is subsequently verified numerically.

B. Spectrum and $|\widehat{L}_{if}|^2$ in a rectangular box

For a rectangle, the energy eigenvalues are

$$\varepsilon_{n_x n_y} = \frac{\pi^2 \hbar^2}{2m} \left(\frac{n_x^2}{L_x^2} + \frac{n_y^2}{L_y^2} \right) \quad (3)$$

We consider rectangles of the same area $A = L_x L_y$ in an ensemble with different values of the ratio $\alpha = L_x^2/L_y^2$. Numerically, we use algebraic numbers for α to reduce accidental level degeneracies. Expressing the energies in terms of the mean level spacing,

$$\Delta = \frac{2\pi \hbar^2}{mA} \quad (4)$$

we find the dimensionless form of the spectrum

$$\varepsilon_{n_x n_y} = \frac{\pi}{4} (\alpha^{-1/2} n_x^2 + \alpha^{1/2} n_y^2) = \frac{\pi}{4} \alpha^{-1/2} (n_x^2 + \alpha n_y^2) \quad (5)$$

For $\alpha \sim 1$, we have a simplified expression for the spectrum

$$\varepsilon_{n_x n_y} \approx \frac{\pi}{4} (n_x^2 + n_y^2) \equiv \frac{\pi}{4} N \quad (6)$$

which will be used in the analytical derivation below [9] (in our numerical work, we also use algebraic α 's close to 1). For an energy $\varepsilon \gg 1$, where the relevant quantities can be described semiclassically, the level i nearest to (and below) ε will be characterized, in general, by a different pair (n_x, n_y) for each α . On the average, the level number \mathcal{N} of level $i = (n_x, n_y)$ is

$$\langle \mathcal{N} \rangle = \varepsilon \gg 1 \quad (7)$$

In what follows, the variations in \mathcal{N} with α are not important. Consequently, we drop $\langle \rangle$ and identify \mathcal{N} with ε .

The matrix element of the orbital angular momentum between the levels $i = (n_x, n_y)$ and $f = (k_x, k_y)$ ($\varepsilon_f > \varepsilon_i$ for definiteness) is given by

$$|\widehat{L}_{if}|^2 = \frac{16}{\pi^4} \left[\begin{aligned} & \frac{n_x^2}{\alpha} \left(\frac{1}{k_x + n_x} + \frac{1}{k_x - n_x} \right)^2 \left(\frac{1}{(k_y + n_y)^2} - \frac{1}{(k_y - n_y)^2} \right)^2 \\ & + \alpha n_y^2 \left(\frac{1}{k_y + n_y} + \frac{1}{k_y - n_y} \right)^2 \left(\frac{1}{(k_x + n_x)^2} - \frac{1}{(k_x - n_x)^2} \right)^2 \\ & - 2n_x n_y \left(\frac{1}{k_x + n_x} + \frac{1}{k_x - n_x} \right) \left(\frac{1}{k_y + n_y} + \frac{1}{k_y - n_y} \right) \\ & \times \left(\frac{1}{(k_x + n_x)^2} - \frac{1}{(k_x - n_x)^2} \right) \left(\frac{1}{(k_y + n_y)^2} - \frac{1}{(k_y - n_y)^2} \right) \end{aligned} \right] \quad (8)$$

where $(k_x - n_x)$ and $(k_y - n_y)$ are odd. Retaining only the terms that contain $(k_x - n_x)$ and $(k_y - n_y)$, we find a simplified form

$$\left| \widehat{L}_{if} \right|^2 \approx \frac{16}{\pi^4} \left[\frac{1}{(k_x - n_x)(k_y - n_y)} \left(\frac{\alpha^{-1/2} n_x}{k_y - n_y} - \frac{\alpha^{1/2} n_y}{k_x - n_x} \right) \right]^2 \quad (9)$$

For levels i and f that are nearest in energy

$$k_x^2 + k_y^2 \approx n_x^2 + n_y^2 \quad (10)$$

and for small $(k_x - n_x)$ and $(k_y - n_y)$, we find

$$n_x(k_x - n_x) \approx -n_y(k_y - n_y) \quad (11)$$

Consequently, for $\alpha \sim 1$,

$$\left| \widehat{L}_{if} \right|^2 \approx \frac{64}{\pi^4} \frac{n_x^2}{(k_x - n_x)^2 (k_y - n_y)^4} \quad (12)$$

Clearly, the magnitude of $\left| \widehat{L}_{if} \right|^2$ is determined by the hierarchy of values $|k_x - n_x|$, $|k_y - n_y|$ such that $\text{sgn}(k_x - n_x) = -\text{sgn}(k_y - n_y)$. Fig. 1 shows $\left| \widehat{L}_{if} \right|^2$ as a functions of \mathcal{N} for a single aspect ratio $\alpha = 8/31^{0.6} \approx 1.01923$. The top straight line corresponds to $k_x - n_x = \pm 1$, $k_y - n_y = \mp 1$. The other two lines correspond, respectively, to $k_x - n_x = \pm 1$, $k_y - n_y = \mp 3$ and $k_x - n_x = \pm 1$, $k_y - n_y = \mp 5$ and $x \leftrightarrow y$ permutations. The slopes of other lines are too small for them to be visible in this plot. Using eqs. (6) and (7), we have $n_x^2 + n_y^2 \approx 4\mathcal{N}/\pi$. Combining this with (11) and substituting into eq. (12), we find

$$\left| \widehat{L}_{if} \right|^2 \approx \frac{128\mathcal{N}}{\pi^5} \times \begin{pmatrix} 1 \\ \frac{1}{45} \\ \frac{1}{325} \end{pmatrix} \begin{pmatrix} \text{for } \pm 1, \mp 1 \\ \text{for } \pm 1, \mp 3 \text{ and } \mp 1, \pm 3 \\ \text{for } \pm 1, \mp 5 \text{ and } \mp 1, \pm 5 \end{pmatrix} \quad (13)$$

for the three lines shown in Fig. 1. As seen from the figure, these straight lines are in excellent agreement with the numerical results.

We emphasize that Fig. 1 should be understood as follows: as i moves up, from one level to the next, $\left| \widehat{L}_{if} \right|^2$ "jumps" - up or down - between the points on straight lines (whose total number is of order \mathcal{N} , with only three shown here), indicating orders of magnitude fluctuations as a function of the position in the spectrum.

C. Spectral average of $\left|\widehat{L}_{if}\right|^2$

It follows from (5) that the greater the range of α , the greater is the spectral (x, y) asymmetry and the higher in spectrum it is necessary to move to eliminate it². On the other hand, keeping α 's close to a fixed value introduces a problem of sampling, which, again, requires higher energies to be considered numerically.³ Thus, there exists an inherent technical difficulty with ensemble averaging in a box. As a practical matter, we take up to 400 values of $\alpha \in [1, 2]$ for the energy range $\varepsilon \sim 10^4 - 10^7$. This choice of parameters proved suitable for ensemble averaging in a numerical part of the study of statistical properties of the energy spectrum itself. [8] However, ensemble averaging with these parameters does not lead to the numerical convergence of $\left\langle \left|\widehat{L}_{if}\right|^2 \right\rangle$.

A portent of this can be already glimpsed from the orders of magnitude fluctuations in $\left|\widehat{L}_{if}\right|^2$ discussed in the preceding subsection. Moreover, if \mathcal{N} is fixed instead but different aspect ratios are considered, the fluctuations of $\left|\widehat{L}_{if}\right|^2$ are as large as a function of α as they are as a function of \mathcal{N} . Consequently, together with α -averaging, an additional spectral averaging over the energy interval $[\varepsilon - E/2, \varepsilon + E/2]$, $E \ll \varepsilon$, is performed to achieve numerical convergence. The interval width is taken to be $\gtrsim \sqrt{\varepsilon}$, which, for the above parameters, increases the sampling range by several orders of magnitude. Interestingly, it also turns out that spectral averaging is amenable to an analytical derivation, which we proceed to outline here.

The key idea in this derivation is that the average of $\left|\widehat{L}_{if}\right|^2$ is dominated by the contribution from the top line in Fig. 1. Numerically, it is clearly seen from Fig.2 where the higher set of points corresponds to averaging over all pairs (i, f) (all lines in Fig. 1), while the lower

²In other words, changes of n_x vs. changes of n_y lead to disparate changes of energy for rectangles whose sides are substantially different. However, this anisotropy is eliminated for an algebraic aspect ratio once above a sufficiently high energy in the spectrum.

³That is, at low energies the spectra for different α 's are very close to each other.

set corresponds to averaging only over the top line in Fig. 1 ($k_x - n_x = \pm 1, k_y - n_y = \mp 1$). The fitting lines for the two sets are given, respectively, by

$$\left\langle \left| \widehat{L}_{if} \right|^2 \right\rangle_{all} = 0.177\sqrt{\mathcal{N}} \quad (14)$$

and

$$\left\langle \left| \widehat{L}_{if} \right|^2 \right\rangle_{top} = 0.172\sqrt{\mathcal{N}} \quad (15)$$

which are remarkably close. Note that we used a combined average over 400 values of $\alpha \in [1, 2]$ and over energy window $E = 4 \times 10^4$. Great sensitivity to the spectral averaging is obvious from Fig. 3 where the interval was reduced to $E = 4 \times 10^2$.

Physical interpretation of these results is as follows. As has been mentioned in the preceding subsection, at a spectral point \mathcal{N} there are $\sim \mathcal{N}$ lines whose slopes can be determined (for small $|k_{x,y} - n_{x,y}|$) via a procedure that resulted in eq. (13). For a given α , as i moves upward from level to level (that is, as \mathcal{N} is increased), $\left| \widehat{L}_{if} \right|^2$ "jumps" between these straight lines. In principle, a "jump" can be from any one of these lines to any other. However, in determining the average, one must remember that not only the slope decreases rapidly from the top line down, but the probability of being on a line also decreases rapidly from $\sim \mathcal{N}^{-1/2}$ on the top line to $\sim \mathcal{N}^{-1}$ over the course of $\sqrt{\mathcal{N}}$ lines. Given this, and in view of the numerical evidence above, we approximate $\left\langle \left| \widehat{L}_{if} \right|^2 \right\rangle$ by the contribution from the top line in Fig. 1 alone. From (13), we find

$$\left\langle \left| \widehat{L}_{if} \right|^2 \right\rangle = \frac{128\mathcal{N}}{\pi^5} P(k_x - n_x = \pm 1, k_y - n_y = \mp 1) \quad (16)$$

$$= \frac{128\mathcal{N}}{\pi^5} P(k_x - n_x = \pm 1) P(k_y - n_y = \mp 1 \mid k_x - n_x = \pm 1) \quad (17)$$

Here $P(k_x - n_x = \pm 1, k_y - n_y = \mp 1)$ and $P(k_y - n_y = \mp 1 \mid k_x - n_x = \pm 1)$ are, respectively, the probability that the nearest energy level pair satisfies the condition $(i, f) = (k_x - n_x = \pm 1, k_y - n_y = \mp 1)$ and a conditional probability that $k_y - n_y = \mp 1$, given that $k_x - n_x = \pm 1$. In what follows, these are evaluated in a series of consecutive steps.

First, we derive the probability distribution function $p(n_x)$. Consider the energy interval defined, in accordance with (6), by the numbers $N_2 > N_1 \gg 1$. A narrow interval is defined as such that

$$\delta \equiv \frac{\Delta N}{N} = \frac{\Delta \mathcal{N}}{\mathcal{N}} \ll 1 \quad (18)$$

where N is the center of the interval and ΔN is its width:

$$N = \frac{N_2 + N_1}{2} = \frac{4}{\pi} \varepsilon = \frac{4}{\pi} \mathcal{N}, \quad \Delta N = N_2 - N_1 = \frac{4}{\pi} E = \frac{4}{\pi} \Delta \mathcal{N} \quad (19)$$

All pair points (n_x, n_y) in this interval are located between the two quarter-circles shown in Fig. 4,

$$N_1 \leq n_x^2 + n_y^2 \leq N_2, \quad n_{x,y} > 0 \quad (20)$$

We propose a simple ansatz whereby $p(n_x) dn_x$ is just the number of states in the interval dn_x , as illustrated by the shaded areas, which gives

$$p(n_x) = \frac{4}{\pi \Delta N} \times \left(\frac{\sqrt{N_2 - n_x^2} - \sqrt{N_1 - n_x^2}}{\sqrt{N_2 - n_x^2}} \right) \left(\begin{array}{l} 0 \leq n_x \leq \sqrt{N_1} \\ \sqrt{N_1} \leq n_x \leq \sqrt{N_2} \end{array} \right) \quad (21)$$

Fig. 5 shows this formula vis-a-vis the numerical evaluation for the same α as in Fig. 1 and for $0.9 \times 10^5 \leq \varepsilon \leq 1.1 \times 10^5$. Clearly, the two are in excellent agreement.

Next, we evaluate the distribution function $p(k_x - n_x)$ by convoluting $p(n_x)$ and $p(k_x)$ under the assumption of no correlations between n_x and k_x :

$$p(k_x - n_x) = \int_0^{\sqrt{N_2}} p(k_x - n_x + t) p(t) dt \quad (22)$$

The resulting formula is very complicated and in Fig. 6 we will only show its plot vis-a-vis numerical evaluation for $0.99 \times 10^6 \leq \varepsilon \leq 1.01 \times 10^6$ for a single α and for an ensemble average over 100 algebraic $\alpha \in [1, 1.25]$. Clearly the agreement between the two is very good. Notice that the dip at zero in the numerical distribution function is due to the fact that the probability of $k_{x,y} - n_{x,y} = 0$ is suppressed for the nearest levels (see, for instance eq. (11) showing that $(k_x - n_x)$ and $(k_y - n_y)$ should be finite and of opposite signs). Notice

also that we treat $(k_x - n_x)$ as a continuous variable and so a deviation from the numerical results should be anticipated for small discrete values of this variable.

As is clear from (17), we only need the probability $P(k_x = n_x \pm 1)$ for our purposes. However, for the reasons just mentioned, we cannot precisely determine it from the distribution obtained via (22) and shown in Fig. 6 by solid line. Consequently, we use an ansatz where this probability is approximated by the area of width ~ 1 near the maximum of the distribution, that is

$$P(k_x - n_x = \pm 1) \approx p(0) \quad (23)$$

where

$$p(0) = \int_0^{\sqrt{N_2}} p^2(t) dt = \frac{32}{3\pi^2\sqrt{N_2}} \frac{1 + (1 - \delta)^{3/2} + \delta K(1 - \delta) - (2 - \delta)E(1 - \delta)}{\delta^2} \quad (24)$$

and K and E are the elliptic functions. Expanding this expression for small δ , while simultaneously replacing N_2 by N , we find

$$p(0) \approx \frac{3 + 8 \ln 2 - 2 \ln \delta}{\pi^2 \sqrt{N}} \quad (25)$$

Fig. 7a shows numerical results for $P(k_x - n_x = \pm 1)$ vis-a-vis eqs. (24) and (25). Fig. 7b also shows $P(k_x - n_x = \pm 1) \sqrt{N}$ vis-a-vis $p(0) \sqrt{N}$. The latter eliminates the main \sqrt{N} dependence and shows that the remainder is a slow-growing function of N . Unfortunately, due to indeterminacy inherently present in our ansatz, it is incapable of exactly describing this function.

To evaluate the conditional probability $P(k_y - n_y = \mp 1 \mid k_x - n_x = \pm 1)$, we notice that by substituting $k_x - n_x = -1$ into (10) and using (6) one finds⁴

$$k_y - n_y = \sqrt{N - (n_x - 1)^2} - \sqrt{N - n_x^2} \quad (26)$$

whereof

⁴Evaluating specifically $P(k_y - n_y = 1 \mid k_x - n_x = -1)$.

$$n_x = \frac{1}{2} \left[1 + (k_y - n_y) \sqrt{\frac{4N - (k_y - n_y)^2}{1 + (k_y - n_y)^2}} \right] \quad (27)$$

in the limit $N \gg 1$. Consequently, using the distribution function (21), we find the distribution function for $p(k_y - n_y \mid k_x - n_x = -1)$ as

$$p(k_y - n_y \mid k_x - n_x = -1) = p(n_x(k_y - n_y)) \frac{dn_x}{d(k_y - n_y)} \quad (28)$$

where $n_x(k_y - n_y)$ is a function given by eq. (27). Combining now eqs. (26)-(28) with eq. (21) we find the analytical form (not shown here due to its complexity) of the conditional probability distribution function and plot it in Fig. 8 vis-a-vis the numerical results.

Before discussing analytical vs. numerical results, we wish to pause briefly on the slight difference between $p(k_y - n_y \mid k_x - n_x = -1)$ and $p(|k_y - n_y| \mid k_x - n_x = 1)$, as seen in Fig. 8. It follows from a more careful examination of eq. (10). Indeed, it should be written as

$$k_x^2 + k_y^2 \approx n_x^2 + n_y^2 + \tilde{\Delta} \quad (29)$$

where $\tilde{\Delta} > 0$ is the separation between the levels. Consequently, (11) should be replaced by

$$n_x(k_x - n_x) \approx -n_y(k_y - n_y) + \frac{\tilde{\Delta}}{2} \quad (30)$$

Obviously then, it is possible to have $k_y - n_y = 0$ when $k_x - n_x = 1$ but not when $k_x - n_x = -1$. This is reflected in numerical curves in Fig. 8 where the conditional probability $p(k_y - n_y \mid k_x - n_x = -1)$ does not have a value at $k_y - n_y = 0$ while $p(|k_y - n_y| \mid k_x - n_x = 1)$ does.

We now turn to a closer analysis of Fig. 8. Obviously, the numerical distribution is much broader than the analytical distribution. The reason for that is that the former was obtained using a large number of α -values whereas the latter was obtained in the approximation where α was set to ~ 1 and hence (6). Clearly, even if the α -values are sufficiently close to 1, as in our simulations, different ensembles are nonetheless sampled for different α 's (for sufficiently high energies, as has been previously mentioned) using the exact formula (5). As a result, the likelihood of larger $|k_y - n_y|$, given that $|k_x - n_x| = 1$, is higher in this case than in our analytical derivation based on (6).

Of note, however, is that for small $|k_y - n_y|$ the analytical curve is well approximated by

$$p(|k_y - n_y| \mid |k_x - n_x| = 1) \approx \frac{2}{\pi(1 + |k_y - n_y|^2)} + \frac{\Delta N}{2\pi N} \xrightarrow{|k_y - n_y|=0} \frac{2}{\pi} + \frac{\Delta N}{2\pi N} \quad (31)$$

We assume that, up to a constant, this gives a good approximation to the dependence on $\Delta N/N = \Delta \mathcal{N}/\mathcal{N}$. Consequently, we propose, similarly to $p(k_x - n_x)$ before, that $P(k_y - n_y = \mp 1 \mid k_x - n_x = \pm 1)$ can be approximated by

$$P(k_y - n_y = \mp 1 \mid k_x - n_x = \pm 1) \approx \text{const} \times p(0 \mid |k_x - n_x| = 1) \quad (32)$$

Fig. 9 shows a plot with an empirical $\text{const} = .225$ used both in "exact" $p(0 \mid |k_x - n_x| = 1)$, obtained from (28), and approximation (31) vis-a-vis the numerical result. Clearly, it provides credence to our ansatz.

D. Summary

The key results of this section are summarized in Figs. 1 and 2 and eqs. (14) and (15):

- Given the energy (the level number) $\simeq \mathcal{N}$, the magnitude of $|\widehat{L}_{if}|^2$ will fall on one of $\sim \mathcal{N}$ lines, such as the three straight line shown in Fig. 1 and given by eqs. (13). Which line specifically it will be on depends on a particular aspect ratio of the rectangle α . Conversely, for a given α , the line it will be on depends on a specific nearest levels pair (i, f) in the vicinity of the energy considered. In other words, $|\widehat{L}_{if}|^2$ experiences orders of magnitude fluctuation both as a function of α and as a function of energy.
- For numerical convergence it was necessary to perform a combined ensemble averaging (over α) and energy averaging (over energy interval $\Delta \mathcal{N} \ll \mathcal{N}$). The result is given by eq. (14) and its magnitude almost entirely derives from the contribution of the top straight line in Fig. 1, $|\widehat{L}_{if}|^2 = 128\mathcal{N}/\pi^5$, as seen by comparison with (15). The probability to find $|\widehat{L}_{if}|^2$ on the top line is $\propto \mathcal{N}^{-1/2}$, which explains why $\langle |\widehat{L}_{if}|^2 \rangle \propto \sqrt{\mathcal{N}}$. It is central to our derivation that the conditional probability $P(k_y - n_y = \mp 1 \mid k_x - n_x = \pm 1)$ only weakly depends on \mathcal{N} , $\sim 0.14(1 + \Delta \mathcal{N}/4\mathcal{N})$.

II. ORBITAL SUSCEPTIBILITY OF A FREE-ELECTRON GAS

A. Introduction

It was recently proposed that, at zero temperature the orbital magnetic susceptibility, of free electrons in disordered systems can be explained by the two level van Vleck response that involves the last occupied (Fermi) level and the first unoccupied level [1], [10]. Whereas for an occasional Fermi level in a given realization of disorder, or for an occasional realization of disorder given a Fermi level close to a fixed energy value, the response can be diamagnetic, in the vast majority of cases it is paramagnetic. This prediction was recently verified numerically in Ref. [11], which also confirmed that both the mean susceptibility and the susceptibility distribution function (mesoscopic fluctuations) can be quite accurately described by the two level model [1], [10].

Orbital susceptibility of rectangles has been previously studied both analytically and numerically [12]- [14]. However, analytically the approach that generally works only at sufficiently high temperature was used and numerically only the rational aspect ratios of rectangles were examined (e.g. squares). Conversely, here we are concerned with a strictly $T = 0$ response for the irrational (algebraic in this numerical evaluation) aspect ratios. Our main conclusion is that, in complete analogy with the disordered systems, both the average and the fluctuations are successfully described by the two level van Vleck response that involves the Fermi level and the first unoccupied level. Furthermore, the largest contribution to the response comes from the values $\left|\widehat{L}_{if}\right|^2$ from the top straight line in Fig. 1, as explained in the preceding Section, while the largest fluctuation occur when, for the points on that line, the energy difference $\varepsilon_f - \varepsilon_i$ between the nearest levels is particularly small.

It will be observed that the orbital susceptibility exhibits a striking absence of self-averaging. While in part it is due to the fact that we evaluate the zero-field response at zero temperature, the underlying physics underscores, nonetheless, that mesoscopic effects are much more pronounced in classically integrable than in classically chaotic systems.

B. Orbital susceptibility of a rectangular box

Using the dimensionless notations, where the energy is measured in units of Δ and the susceptibility in units of μ_B^2/Δ , we find the total orbital susceptibility as follows:

$$\chi_{tot} = - \sum_{i=1}^{\mathcal{N}} \frac{2\pi \langle i | x^2 + y^2 | i \rangle}{A} + \sum_{i=1}^{\mathcal{N}} \sum_{f=\mathcal{N}+1}^{\infty} \frac{2 |\widehat{L}_{if}|^2}{\varepsilon_f - \varepsilon_i} \quad (33)$$

where ε_i , $i = (n_x, n_y)$, is the unperturbed (zero-field) spectrum (5). While the Landau gauge was used in this expression, the final result is gauge-independent (for a discussion, see Ref. [11]). The diamagnetic matrix elements are easily calculated and are given by

$$\langle i | x^2 + y^2 | i \rangle = \frac{A}{12} \left[\alpha^{1/2} \left(1 - \frac{6}{\pi n_x^2} \right) + \alpha^{-1/2} \left(1 - \frac{6}{\pi n_y^2} \right) \right] \quad (34)$$

Fig. 10 shows the result of numerical evaluation of $\langle \chi_{tot} \rangle$ plotted as a function of \mathcal{N} , vis-a-vis $\left\langle 2 |\widehat{L}_{if}|^2 (\varepsilon_f - \varepsilon_i)^{-1} \right\rangle$, where ε_i and ε_f are now limited to the Fermi level and the first unoccupied level, $i = \mathcal{N}$, $f = \mathcal{N} + 1$. This is motivated by the surmise that the contributions of the two sums in eq. (33) - diamagnetic and paramagnetic - largely cancel each other over the Fermi sea and the total susceptibility, on average, can be explained by a single term in the van Vleck sum, namely, the one between the last occupied and the first unoccupied levels. (The analogous surmise in disordered systems [1], [10] had been already verified numerically [11].) The subset of the latter, $\left\langle 2 |\widehat{L}_{if}|^2 (\varepsilon_f - \varepsilon_i)^{-1} \right\rangle_{top}$, with the contributions only from the top line in Fig. 1 is also shown. While the difference in the distribution function of $(\varepsilon_f - \varepsilon_i)$ on the top line relative to the Poissonian should be noted (and will be discussed in a separate publication), the dominance of the $k_x - n_x = \pm 1, k_y - n_y = \mp 1$ contribution to $|\widehat{L}_{if}|$ suggests that the top line should dominate the contribution from the $i = \mathcal{N}$, $f = \mathcal{N} + 1$ term also. Finally, $2 \left\langle |\widehat{L}_{if}|^2 \right\rangle \langle (\varepsilon_f - \varepsilon_i)^{-1} \rangle$, is also shown in Fig. 10, where $\left\langle |\widehat{L}_{if}|^2 \right\rangle$ is shown in Fig. 2 and approximated by eq. (14) and $\langle (\varepsilon_f - \varepsilon_i)^{-1} \rangle$ is evaluated numerically and found to be (in units of Δ^{-1})

$$\left\langle \frac{1}{\varepsilon_f - \varepsilon_i} \right\rangle \approx 15.5 \quad (35)$$

Despite a combined averaging over 400 α 's and energy interval 4000-wide, the absence of self averaging is still evident in this plot. (To further emphasize the predominance of large fluctuations, in Fig. 11 we show the same $\langle\chi_{tot}\rangle$ as in Fig. 10 vis-a-vis $\langle\chi_{tot}\rangle$ that was obtained for the same α -ensemble but whose energy averaging was performed over intervals 10 times narrower.) On the other hand, our surmise that the two level van Vleck paramagnetism accurately describes the average orbital response is evident from Fig. 10 as the structure of $\langle\chi_{tot}\rangle$ vs. \mathcal{N} is well reproduced by the nearest level contributions alone; the difference between the two are the contributions from the terms in the double-sum of (33) that are due to the levels further below and above the Fermi level.

The large value of $\langle(\varepsilon_f - \varepsilon_i)^{-1}\rangle$ in (35) is readily understood from the exponential (Poissonian) distribution function of the level spacings [5], [6], $p(\varepsilon_f - \varepsilon_i) = \exp[-(\varepsilon_f - \varepsilon_i)]$, whereof

$$\left\langle \frac{1}{\varepsilon_f - \varepsilon_i} \right\rangle = \int_{\epsilon}^{\infty} \frac{\exp(-x)}{x} dx = \ln \frac{1}{\epsilon} \quad (36)$$

where ϵ is a cut-off. Since we evaluate the zero field response at zero temperature, the cut-off is the smallest spacing observed for the values of α and energies considered here, which happens to be $\sim 10^{-7}$ (the mean level spacing being 1). As already mentioned, the distribution function of the level spacings on the top line of Fig. 1 will be discussed elsewhere, however, it turns out that $\langle(\varepsilon_f - \varepsilon_i)^{-1}\rangle$ is also formally divergent and, for the parameters used here, numerical evaluation gives $\langle(\varepsilon_f - \varepsilon_i)^{-1}\rangle \approx 12.5$. It should be pointed out however that in reality, even at zero temperature, the magnetic field itself introduces a natural cut-off; for disordered systems this was discussed in Ref. [10].

We now turn to the study of fluctuations. To understand the nature of mesoscopic fluctuations, we investigate the energy differences between the nearest levels. We limit our consideration to the top line in Fig. 1 as it dominates the response, both in terms of the mean and the fluctuations. Figs. 12-14 show plots of $(\varepsilon_f - \varepsilon_i)^{-1}$ and $\varepsilon_f - \varepsilon_i$ as a function of \mathcal{N} for three particular values of α , respectively $\alpha_1 = 457^{0.855}/185 \approx 1.01638$, $\alpha_2 = 911^{0.755}/150 \approx 1.14379$, and $\alpha_3 = 643^{0.655}/63 \approx 1.09657$. First, we notice the existence

of very large values of $(\varepsilon_f - \varepsilon_i)^{-1}$, which are the source of very large mesoscopic fluctuations. Second, we notice patterns in the structure of $(\varepsilon_f - \varepsilon_i)^{-1}$ and $\varepsilon_f - \varepsilon_i$ as a function of \mathcal{N} . Lastly, we notice that the size of the peaks and the pattern structure is very strongly α -dependent.

It turns out that the patterns in Figs. 12-14, as well as the size and the location of the peaks, can be determined analytically. Considering for simplicity the case of $\alpha = 1 + \beta$, $0 < \beta < 1/2$, we find

$$\frac{4\alpha^{1/2}}{\pi} (\varepsilon_f - \varepsilon_i) = \begin{pmatrix} 2(n_x - n_y + 1) - \beta(2n_y - 1) \\ 2(n_y - n_x + 1) + \beta(2n_y + 1) \end{pmatrix} \begin{pmatrix} k_x - n_x = 1, k_y - n_y = -1 \\ k_x - n_x = -1, k_y - n_y = 1 \end{pmatrix} \quad (37)$$

The algebraic β can be represented as a series

$$\beta = \frac{1}{p} + \frac{1}{q} + \frac{1}{r} + \dots \quad (38)$$

where $p > 2$, $|q| > p^2$, $|r| > q^2$, \dots are integers. The series can be truncated

$$\begin{aligned} \beta &= \frac{1}{p} + \eta \\ \beta &= \frac{1}{p} + \frac{1}{q} + \eta \\ \beta &= \frac{1}{p} + \frac{1}{q} + \frac{1}{r} + \eta \\ &\dots \end{aligned} \quad (39)$$

where η is the residual algebraic number. For β 's corresponding to Figs. 12-14, the truncated series are as follows:

$$\begin{aligned} \beta_1 &= \frac{1}{61} - \frac{1}{81672} - 5.1 \times 10^{-11} \\ \beta_2 &= \frac{1}{7} + \frac{1}{1076} + \frac{1}{2616460} + 5.6 \times 10^{-13} \\ \beta_3 &= \frac{1}{10} - \frac{1}{292} - \frac{1}{472427} \times 10^{-13} \end{aligned} \quad (40)$$

Specifics of truncation depend on the position in the energy spectrum, to which numerical analysis is extended, and on the values of integers p, q, r, \dots , as explained below.

The key to understanding the spacings structure in Figs. 12-14 is that it can be completely described by as few as the first two rational numbers in the approximation of β (39).

(Only for the very rare occurrences of degeneracy, $\varepsilon_f - \varepsilon_i = 0$, does the residual term η needs to be considered.) Therefore, we turn to the analysis of the interplay between the rational numbers. We begin with the spacings structure for $\beta = p^{-1}$, shown in Figs. 15 for $p = 100$. Analytically, (37) yields the following series of straight lines, as a function of n_y :

$$\begin{aligned} \frac{4\alpha^{1/2}}{\pi}(\varepsilon_f - \varepsilon_i) &= 2C + 2 + \frac{1}{p} - \frac{2}{p}n_y, \left(\begin{array}{c} pC + \frac{1}{2} \leq n_y \leq p(C+1) + \frac{1}{2} \\ C = 0, 1, 2, \dots \end{array} \right), k_x - n_x = 1, k_y - n_y = -1 \\ & \\ \frac{4\alpha^{1/2}}{\pi}(\varepsilon_f - \varepsilon_i) &= -2C + 2 + \frac{1}{p} + \frac{2}{p}n_y, \left(\begin{array}{c} p(C-1) - \frac{1}{2} \leq n_y \leq pC - \frac{1}{2} \\ C = 1, 2, 3, \dots \end{array} \right), k_x - n_x = -1, k_y - n_y = 1 \end{aligned} \quad (41)$$

Here $C = n_x - n_y$ is a non-negative integer, due to the choice of $\alpha > 1$, and the limits on n_y are determined from the condition

$$0 \leq \frac{4\alpha^{1/2}}{\pi}(\varepsilon_f - \varepsilon_i) \leq 2 \quad (42)$$

where the second inequality can be understood from the fact that changing C by 1 changes $4\alpha^{1/2}(\varepsilon_f - \varepsilon_i)/\pi$ by 2, making it extremely unlikely that ε_f is the nearest level to ε_i if the second constraint in (42) is not satisfied; this is also confirmed numerically. Furthermore, the maxima in Fig. 15a (minima in Fig. 15b) are found as follows:

$$\begin{aligned} \frac{4\alpha^{1/2}}{\pi}(\varepsilon_f - \varepsilon_i)_{\min} &= \frac{1}{p}, \text{ when } \left(\begin{array}{c} n_y = p(C+1) \\ C = 0, 1, 2, \dots \end{array} \right), k_x - n_x = 1, k_y - n_y = -1 \\ & \\ \frac{4\alpha^{1/2}}{\pi}(\varepsilon_f - \varepsilon_i) &= \frac{1}{p}, \text{ when } \left(\begin{array}{c} n_y = p(C-1) \\ C = 2, 3, 4, \dots \end{array} \right), k_x - n_x = -1, k_y - n_y = 1 \end{aligned} \quad (43)$$

Combining eqs. (41) and (43) with

$$\mathcal{N} = \frac{\pi(n_x^2 + \alpha n_y^2)}{4\alpha^{1/2}} \quad (44)$$

completely describes the spacings structure as a function of \mathcal{N} , for instance, as shown in Figs. 15.

We turn to the next approximation in (39), $\beta = p^{-1} + q^{-1}$. For simplicity, we will consider only $k_x - n_x = 1, k_y - n_y = -1$ and $q < 0$. In this case, the spacings structure is described by the following equations:

$$\frac{4\alpha^{1/2}}{\pi}(\varepsilon_f - \varepsilon_i) = \frac{2t + 2p + 1}{p} + \frac{1 - 2n_y}{q}, \left(\begin{array}{l} 1 \leq n_y \leq \frac{(2t+1)q+p}{2p}, -p \leq t < 0 \\ \frac{(2t+2p+1)q+p}{2p} \leq n_y \leq \frac{(2t+1)q+p}{2p}, t \leq -p-1 \end{array} \right) \quad (45)$$

Here t is an integer and possible n_y 's are subject to the constraint

$$t = pC - n_y \quad (46)$$

where, as before, $C = n_x - n_y \geq 0$ is an integer. The minima of the structure are found at

$$n_y = p \left\lfloor \frac{t}{p} + \frac{(2t + 2p + 1)q}{2p^2} + \frac{1}{2p} + 1 \right\rfloor - t, \quad t \leq -p - 1 \quad (47)$$

where the $\lfloor \rfloor$ brackets denote the floor (integer value) function. Together, eqs. (44)-(47) completely describe the spacings structure in Figs. 12. Furthermore, generalization to the next iteration, $\beta = p^{-1} + q^{-1} + r^{-1}$, is straightforward and accounts for Figs. 13 and 14.

Semiquantitatively, the peak structure of $(\varepsilon_f - \varepsilon_i)^{-1}$ along \mathcal{N} axis is summarized below. In what follows, we will discuss the spacings structure as a function of $2n_y$, which is easily converted to that of \mathcal{N} , as explained above. The upper limit of \mathcal{N} , vs. the values of p, q, r, \dots in approximation of a particular $\alpha(\beta)$, determines how many terms is necessary to keep in (39). Namely, q^{-1} enters in (39) when $2n_y \gtrsim q/p$ and r^{-1} enters when $2n_y \gtrsim r/q$; this is illustrated by (40), as applied to Figs. 12-14. Noting that peaks correspond to the end points (negative slope) and first points (positive slope) of the straight lines given by eqs. (41), (45), etc., and calling the distance between the tallest peaks "period," we find the following⁵:

- Peaks of p^{-1} : "period" $\sim p$; height of peaks is p .
- Peaks of $p^{-1} + q^{-1}$: (assuming that pq and $p+q$ have no common factor) period $\sim 2pq$, with $\sim p^2$ peaks per period separated by distance $\sim 2q/p$; upper limit of peaks is pq

⁵It should be emphasized that not all peaks are observed for the \mathcal{N} considered; in fact it is possible to not observe any peaks at all, in which case the maxima of the structure are determined by the end points of the interval on the \mathcal{N} axis.

(heights of peaks are $pq, pq/3, \dots, \sim q/p$, or in reverse order), for $p + q$ odd, and ∞ ($\infty, pq/2, pq/4, \dots, \sim q/p$) for $p + q$ even (∞ indicates level degeneracy, $\varepsilon_f - \varepsilon_i = 0$, so that the residual term η must be considered in (39)).

- Peaks of $p^{-1} + q^{-1} + r^{-1}$: (assuming that pqr and $pq + qr + pr$ have no common factor) period $\sim 2pqr$, with $\sim p^2q^2$ peaks per period separated by distance $\sim 2r/pq$; upper limit of peaks is pqr (heights of peaks $pqr, pqr/3, \dots, \sim r/qp$, or in reverse order), for $pq + qr + pr$ odd, and ∞ ($\infty, pqr/2, pqr/4, \dots, \sim r/qp$) for $pq + qr + pr$ even.

C. Summary

The central result of this section is shown in Fig. 10. It demonstrates that the mean zero-temperature, zero-field orbital magnetic susceptibility of a free electron gas in a rectangular box can be explained in terms of a two-level van Vleck response - that of the last occupied (Fermi) and the first unoccupied levels. Furthermore, it is dominated by the contributions from the top line in Fig. 1, namely $k_x - n_x = \pm 1, k_y - n_y = \mp 1$, which is also the largest contributor to $\left\langle \left| \hat{L}_{if} \right|^2 \right\rangle$ discussed in the preceding section. In fact, the mean value of susceptibility is reasonably well described by $\left\langle \left| \hat{L}_{if} \right|^2 \right\rangle \left\langle (\varepsilon_f - \varepsilon_i)^{-1} \right\rangle$, where $\left\langle (\varepsilon_f - \varepsilon_i)^{-1} \right\rangle$ is large due to the absence of correlations for small level separations.

It is also evident that the orbital susceptibility is largely a non self-averaging quantity, as seen from Figs. 10 and 11. This is due to the existence of huge variations in inverse level spacings, which, in turn, allow for such large contributions that may singularly outweigh the totality of more typical contributions in the average response. Such variations were explained in terms of a decomposition of algebraic aspect ratios into rational numbers, whose interplay in (39) is crucial for understanding the peaks of $(\varepsilon_f - \varepsilon_i)^{-1}$. It must be borne in mind, however, that this feature of the orbital susceptibility is very fragile with respect to perturbations and that mesoscopic fluctuations will be suppressed at finite temperatures (or even by finite values of the magnetic field); we intend to address this problem elsewhere.

III. CONCLUSIONS

The most striking feature revealed here is the non-self-averaging property of physical quantities in a rectangular box, which represents a class of integrable billiard problems. We had previously discussed [8] the persisting long-range correlations in the semiclassical energy spectrum of this system. These correlations are more complex than those in classically chaotic (disordered) systems [5]- [7]. In particular, we discussed the large, non-decaying oscillations of the level number variance on an energy interval as a function of the interval width. Similarly, we find that mesoscopic fluctuations here are much more pronounced than in classically chaotic systems. For instance, while eqs. (1) and (2) point to the same order of magnitude in a ballistic disordered system, $\ell \sim L$, and a rectangular billiard, the latter will have much larger fluctuations (we have discussed the difficulties with averaging in text).

The one similarity that stands out for both integrable and chaotic systems is that both the average orbital susceptibility of the free electron gas and its fluctuations can be well described by a two level van Vleck response that couples the last occupied (Fermi) and the first unoccupied levels. For disordered systems, this has been demonstrated previously in Refs. [1], [10], and [11] and for an integrable case in this work. The difference, however, is that in disordered systems the non-self-averaging effects are less pronounced: in the absence of cut-offs (temperature, finite magnetic field, etc.), the average is well defined and only the higher cumulants are divergent. In a rectangular box, even the average is already ill-defined, as pointed out in discussion of eq. (36).

Our next step will be to investigate the effect of temperature on the orbital magnetism of integrable systems. Towards this end, we will apply Imry's formalism, which allows to express the average response in terms of the level correlation function. [15] For rectangles, the latter is now well understood, including as function of magnetic field. [8] This formalism works well at sufficiently high temperature and should provide an insight into the scales at which the transition to the zero-temperature limit, discussed here, occurs (as was done for disordered systems [1]). Our results will then be discussed vis-a-vis previous works [13], [14].

IV. FIGURE CAPTIONS

1. Figure 1

$\left|\widehat{L}_{if}\right|^2$ vs. \mathcal{N} ($\varepsilon = \mathcal{N}$ in our approximation). The number of lines, where the value of $\left|\widehat{L}_{if}\right|^2$ might fall, increases with \mathcal{N} . For a given \mathcal{N} (more precisely, for a given level i), $\left|\widehat{L}_{if}\right|^2$ is on one of the lines, depending on α . As, for any given α , \mathcal{N} is increased ($i \rightarrow i+1 = f$, $f \rightarrow f+1$), $\left|\widehat{L}_{if}\right|^2$ "jumps" to another line. The lines are the same regardless of α . For illustration, we present numerical results for $\alpha = 8/31^{0.6} \approx 1.01923$. Equations for the three straight lines shown here are given by (13).

2. Figure 2

Numerical average of $\left\langle \left|\widehat{L}_{if}\right|^2 \right\rangle$ vs. \mathcal{N} vis-a-vis the fits (14) and (15). A combined average over 400 algebraic values of $\alpha \in [1, 2]$ and over the energy interval $[\mathcal{N} - 2 \times 10^4, \mathcal{N} + 2 \times 10^4]$ was used. The bottom line and fit correspond to the contribution from the top line only in Fig. 1 ($k_x - n_x = \pm 1, k_y - n_y = \mp 1$).

3. Figure 3

Same as the top set of dots in Fig 2 vs. the result of averaging over a narrower interval, $[\mathcal{N} - 2 \times 10^2, \mathcal{N} + 2 \times 10^2]$.

4. Figure 4

Shaded areas represent the probabilities $p(n_x) dn_x$.

5. Figure 5

Distribution function $p(n_x)$ vs. n_x : analytical result with $p(n_x)$ given by eq. (21) vis-a-vis numerical data for $0.99 \times 10^5 \leq \varepsilon \leq 1.01 \times 10^5$ and the same α as in Fig. 1.

6. Figure 6

$p(k_x - n_x)$ vs. $(k_x - n_x)$: analytical result obtained via (22) vis-a-vis numerical data for $0.99 \times 10^6 \leq \varepsilon \leq 1.01 \times 10^6$ for the same α as in Fig. 1 and for an ensemble average over 100 algebraic $\alpha \in [1, 1.25]$.

7. Figure 7a

Probability $P(k_x - n_x = \pm 1)$ vs. \mathcal{N} : analytical ansatz based on (23) and (24) and on its approximation (25) (solid lines) vis-a-vis numerical data.

8. Figure 7b

$P(k_x - n_x = \pm 1) \sqrt{\mathcal{N}}$ vs. \mathcal{N} : same as Fig.7a, but with the main dependence, $\propto \mathcal{N}^{-1/2}$, eliminated.

9. Figure 8

Distribution functions of conditional probability $p(k_y - n_y | k_x - n_x = -1)$ and $p(|k_y - n_y| | k_x - n_x = 1)$: analytical result obtained via (28) vs. numerical data. Notice that for the latter $p(0 | k_x - n_x = -1) = 0$ while $p(0 | k_x - n_x = 1) \neq 0$, as explained in text.

10. Figure 9

Conditional probability $P(k_y - n_y = \mp 1 | k_x - n_x = \pm 1)$ vs. \mathcal{N} : an ansatz based on $0.225 \times p(0 | |k_x - n_x| = 1)$ and its approximation $0.14 \times (1 + \Delta N/4N)$ (solid lines) vis-a-vis numerical data.

11. Figure 10

Total magnetic susceptibility, evaluated via (33) and (34) - top set of dots. $\left\langle 2 \left| \widehat{L}_{if} \right|^2 (\varepsilon_f - \varepsilon_i)^{-1} \right\rangle$, where ε_i and ε_f are the Fermi level and the first unoccupied level respectively - middle set of dots. $\left\langle 2 \left| \widehat{L}_{if} \right|^2 (\varepsilon_f - \varepsilon_i)^{-1} \right\rangle_{top}$, where ε_i and ε_f are the Fermi level and the first unoccupied level such that $k_x - n_x = \pm 1, k_y - n_y = \mp 1$ (top line in Fig. 1) - bottom set of dots. $2 \left\langle \left| \widehat{L}_{if} \right|^2 \right\rangle \langle (\varepsilon_f - \varepsilon_i)^{-1} \rangle$ with $\left\langle \left| \widehat{L}_{if} \right|^2 \right\rangle$ given by the top set of dots in Fig. 2 and $\langle (\varepsilon_f - \varepsilon_i)^{-1} \rangle \approx 15.5$. A combined average over 400 algebraic values of $\alpha \in [1, 2]$ and over the energy interval $[\mathcal{N} - 2 \times 10^3, \mathcal{N} + 2 \times 10^3]$ was used.

12. Figure 11

Large dots same as top dots in Fig. 10. Small dots - a combined average over same 400 algebraic values of $\alpha \in [1, 2]$ but over the narrower energy interval $[\mathcal{N} - 2 \times 10^2, \mathcal{N} + 2 \times 10^2]$.

13. Figure 12a

$(\varepsilon_f - \varepsilon_i)^{-1}$ vs. \mathcal{N} for $\alpha_1 = 457^{0.855}/185 \approx 1.01638$, where ε_i and ε_f are the nearest levels such that $k_x - n_x = \pm 1, k_y - n_y = \mp 1$. $\beta = \alpha - 1$ is decomposed according to the first eq. (40). Coordinates of point A are (718964, 25443.6) and can be described analytically by (45) with $t = -62$, $C = n_x - n_y = 10$ and $n_y = 672$.

14. Figure 12b

Same as Figure 12a, shows $\varepsilon_f - \varepsilon_i$ vs. \mathcal{N} and point A.

15. Figure 13a

$(\varepsilon_f - \varepsilon_i)^{-1}$ vs. \mathcal{N} for $\alpha_2 = 911^{0.755}/150 \approx 1.14379$ and β given by second eq. (45) Points A-D have been examined; they can be described analytically by equations that are

an extension of (45) to include the next iteration in (39).

16. Figure 13b

Same as Figure 13a, shows $\varepsilon_f - \varepsilon_i$ vs. \mathcal{N} and points A - D .

17. Figure 14a

$(\varepsilon_f - \varepsilon_i)^{-1}$ vs. \mathcal{N} for $\alpha_3 = 643^{0.655}/63 \approx 1.09657$ and β given by third eq. (45). Points A and B have been examined; they can be described analytically by equations that are an extension of (45) to include the next iteration in (39).

18. Figure 14b

Same as Figure 14a, shows $\varepsilon_f - \varepsilon_i$ vs. \mathcal{N} and points A and B .

19. Figure 15a

$(\varepsilon_f - \varepsilon_i)^{-1}$ vs. \mathcal{N} for the rational aspect ratio $\alpha = 1.01$. All the points are described analytically by eqs. (41) with $p = 100$. The maxima, denoted by A and B (two points each, corresponding to increasing and decreasing functions of \mathcal{N} in (41)) are given by eqs. (43).

20. Figure 15b

Same as Figure 15a, shows $\varepsilon_f - \varepsilon_i$ vs. \mathcal{N} and points A and B .

REFERENCES

- [1] R. A.. Serota, Solid State Commun. **117**, 99 (2001).
- [2] K. A.. Matveev, L. I.. Glazman, A. I.. Larkin, Phys. Rev. Lett. **85**, 2789 (2000).
- [3] E. A.. Shapoval, Sov. Phys. JETP **20**, 675 (1965)
- [4] L. P.. Gor'kov and G. M.. Eliashberg, Sov. Phys. JETP **21** , 940 (1965).
- [5] Martin C. Gutzwiller ” *Chaos in classical and quantum mechanics*” (Springer-Verlag, 1990)
- [6] T. A. Brody, J. Flores, J. B. French, P. A. Mello, A. Pandey, and S. S. M. Wong, Rev. Mod. Phys. **53**, 385 (1981).
- [7] Konstantin Efetov ” *Supersymmetry in disorder and chaos*” (Cambridge University Press, 1997) and references therein.
- [8] J. M. A. S. P. Wickramasinghe and R. A. Serota, cond-mat/0306110 (2003); J. M. A. S. P. Wickramasinghe, B. Goodman, and R. A. Serota, to be published in Phys. Rev. E (2005).
- [9] M. V. Berry, Proc. R. Soc. Lond. **A400**, 229 (1985).
- [10] R. A. Serota, Source: Physica **E15**, 211 (2002).
- [11] M. Goldstein, R. Berkovits, Phys. Rev. **B69**, 035323 (2004).
- [12] J. M. van Ruitenbeek and D. A. van Leeuwen, Phys. Rev. Lett. **67**, 640 (1991).
- [13] F. von Open, Phys. Rev. **B50**, 17151 (1994).
- [14] K. Richter, D. Ullmo, and R. A. Jalabert, Phys. Rep. **276**, 1 (1996).
- [15] S. Sitotaw and R. A. Serota, Physica Scripta **60**, 283 (1999) and references therein.

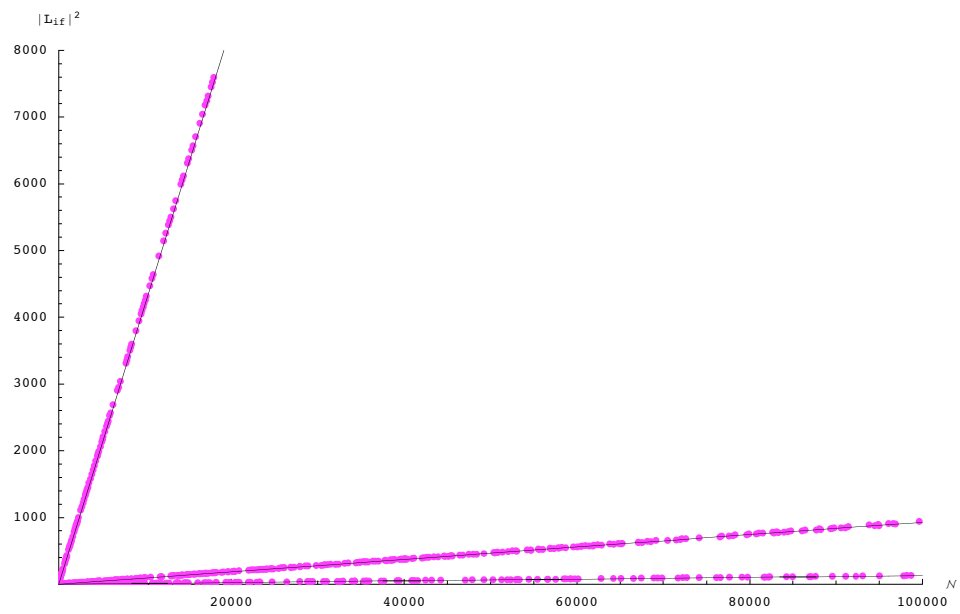


Figure 1

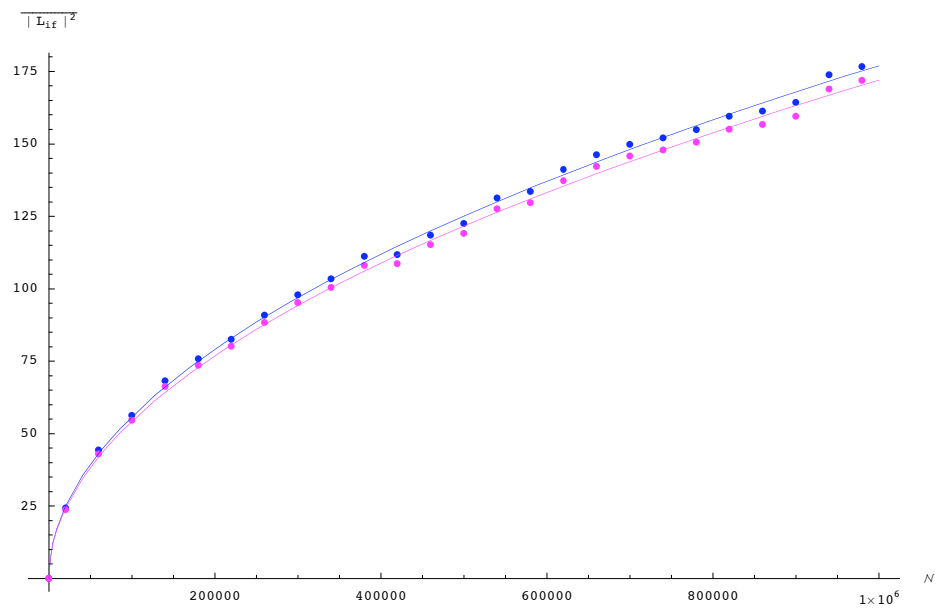


Figure 2

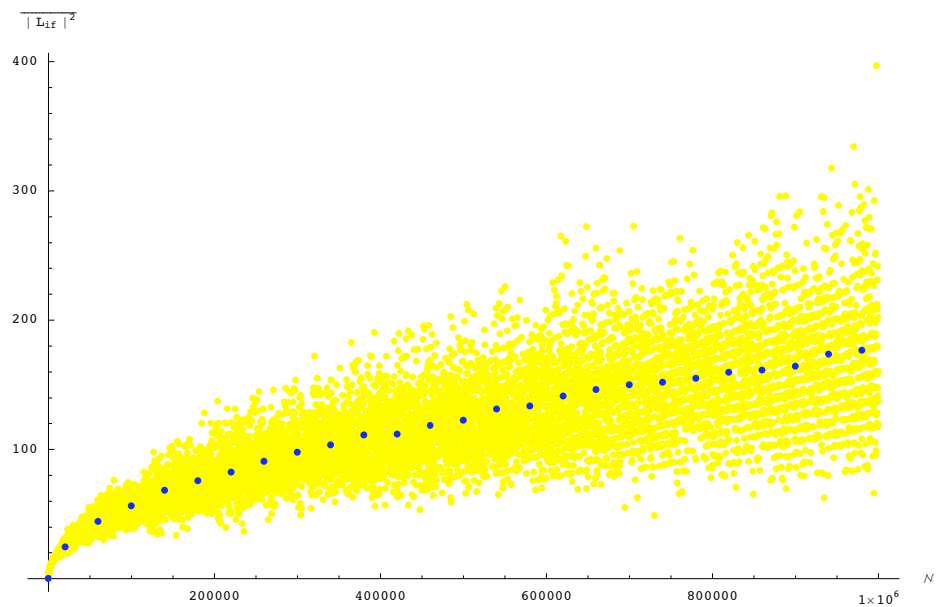


Figure 3

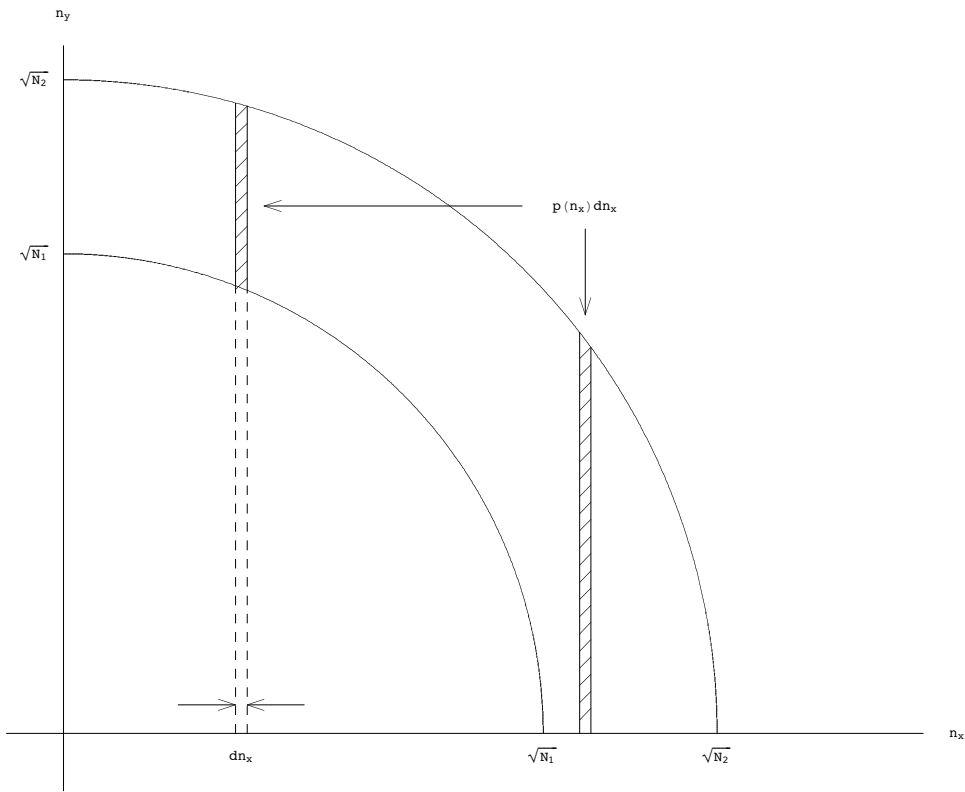


Figure 4

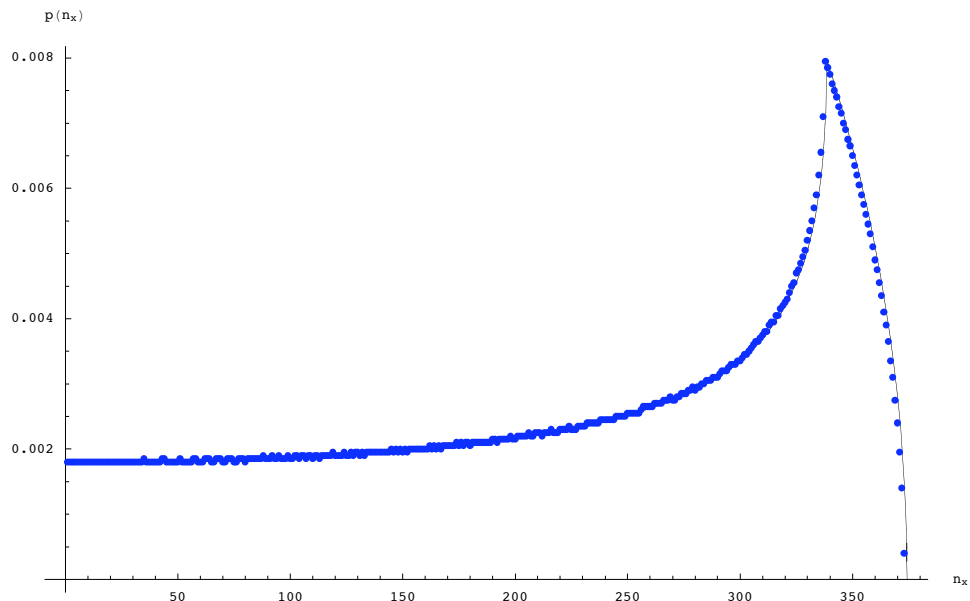


Figure 5

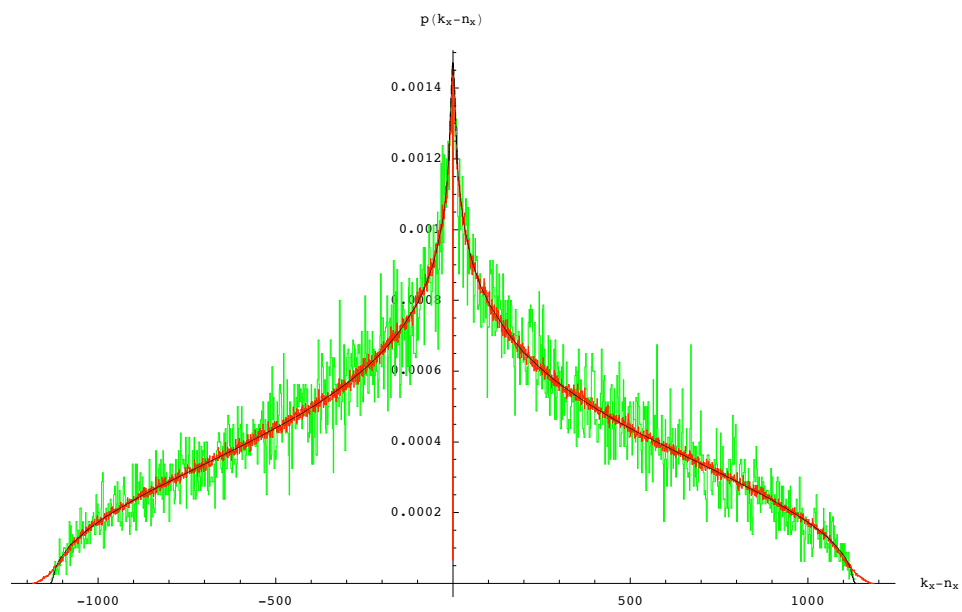


Figure 6

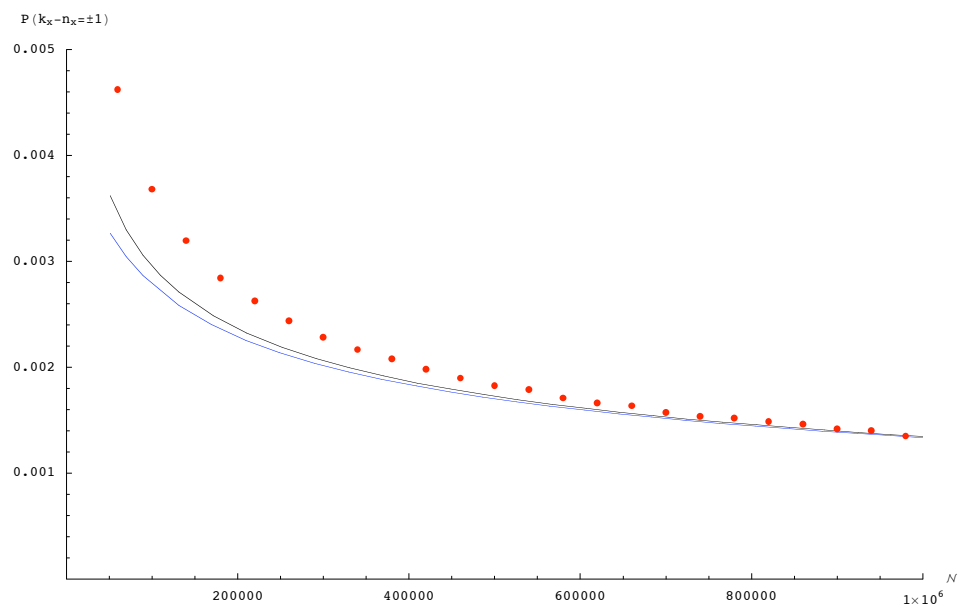


Figure 7a

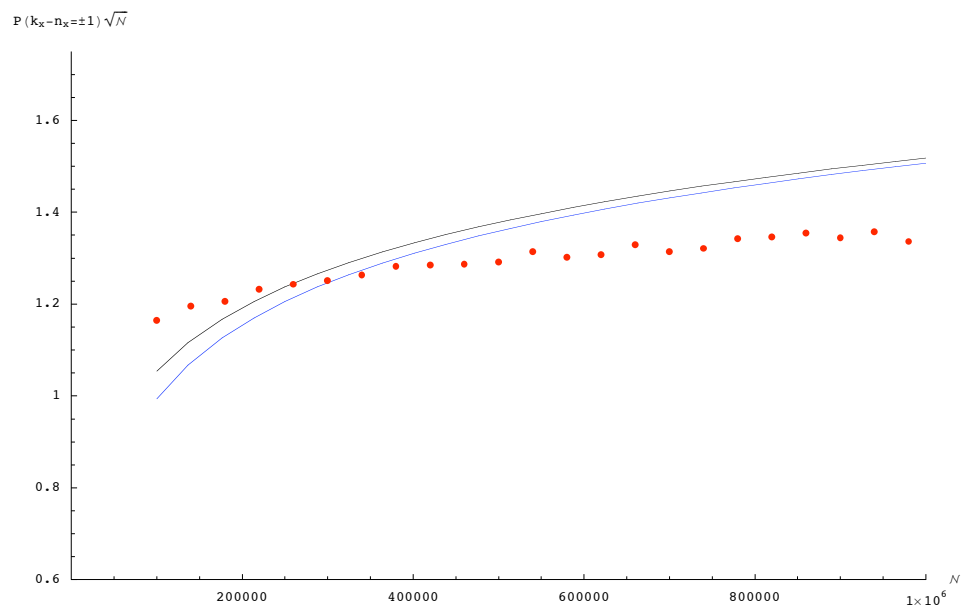


Figure 7b

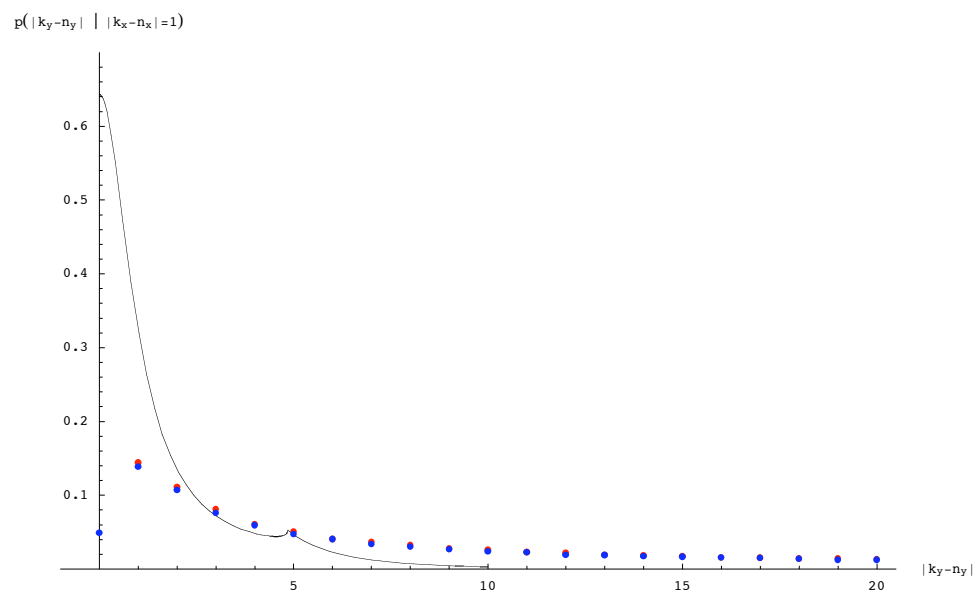


Figure 8

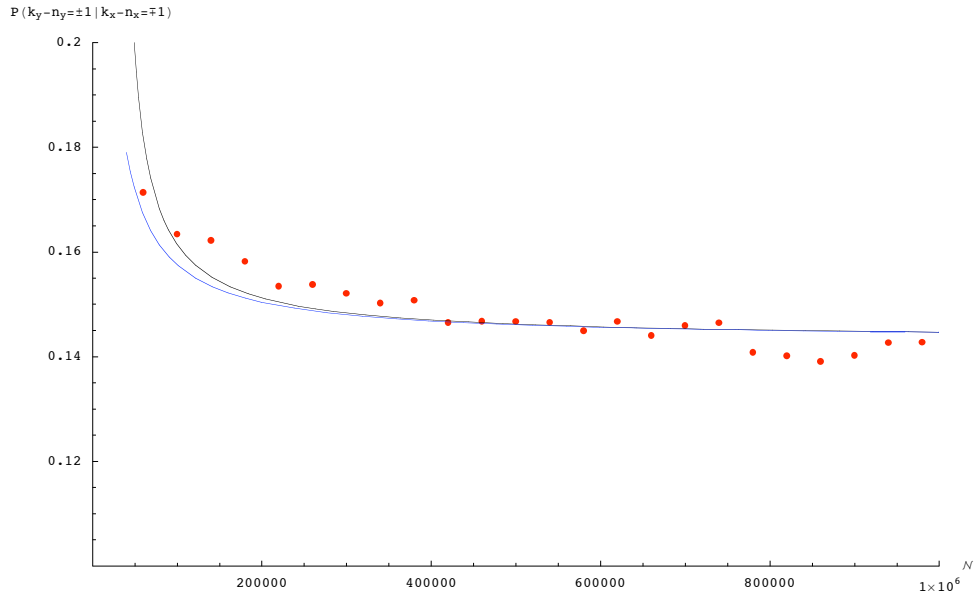


Figure 9

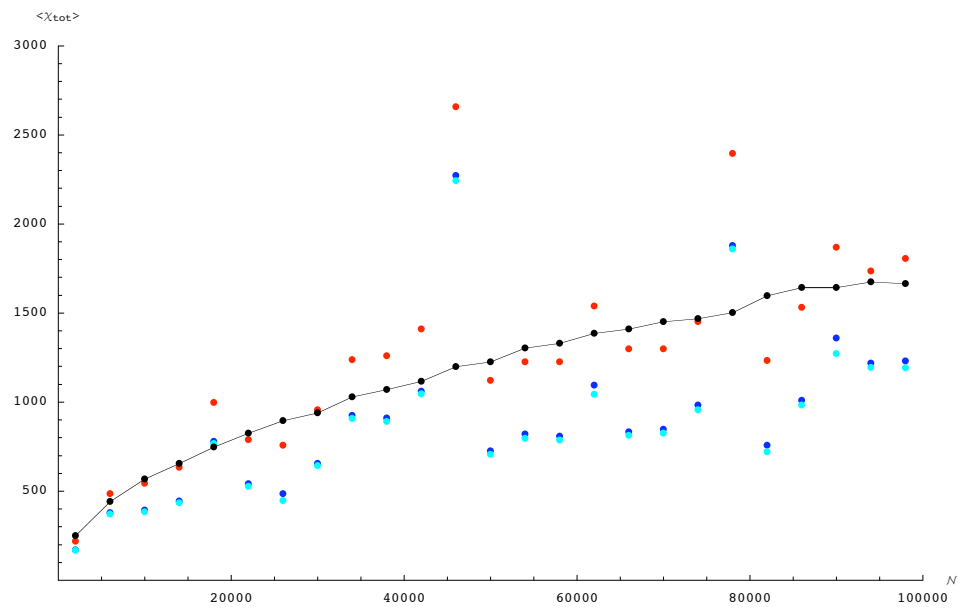


Figure 10

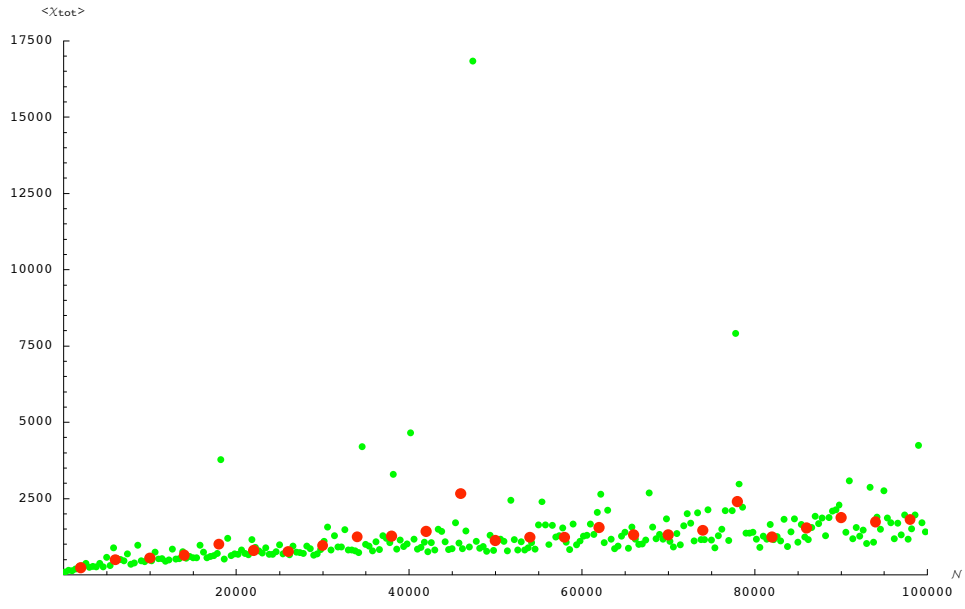


Figure 11

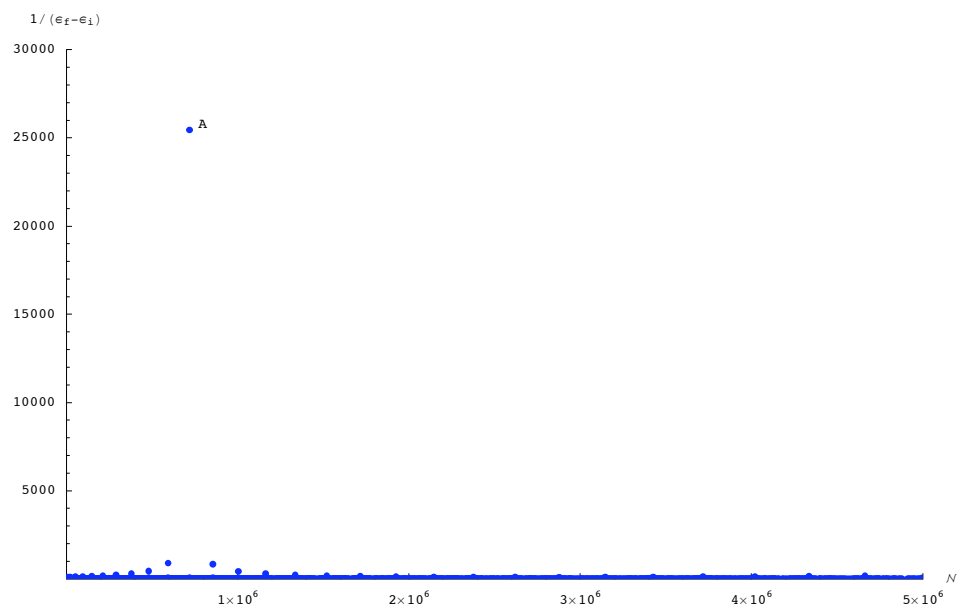


Figure 12a

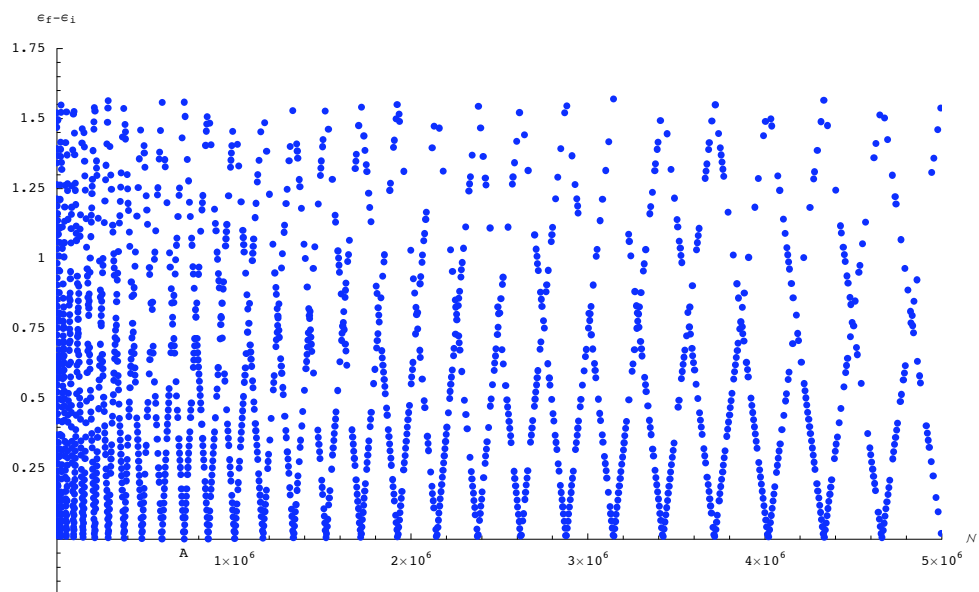


Figure 12b

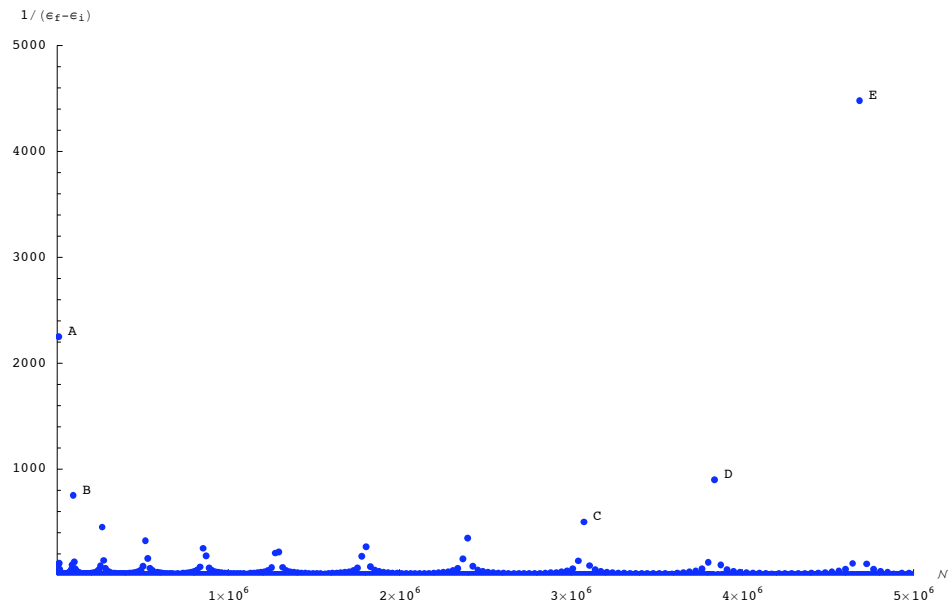


Figure 13a

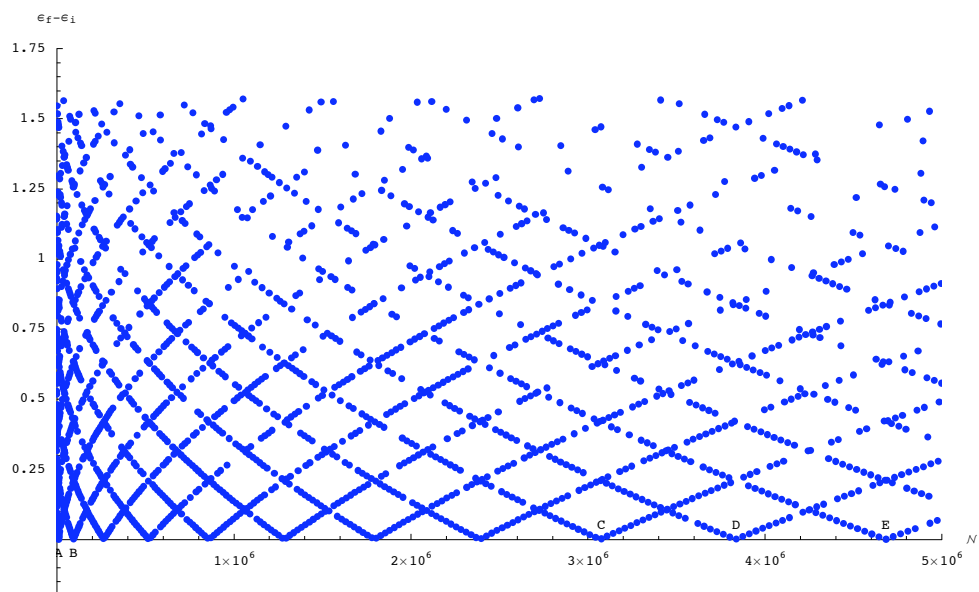


Figure 13b

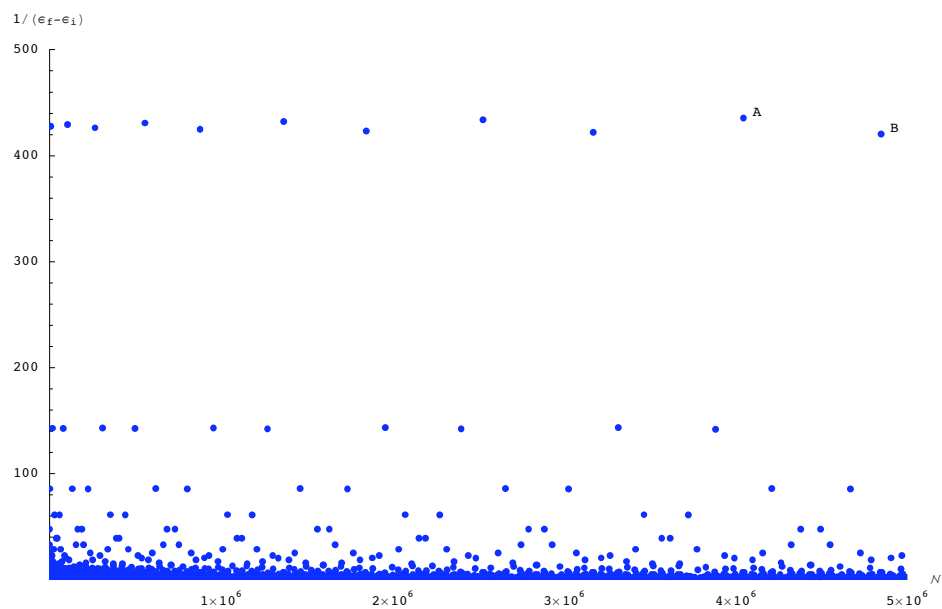


Figure 14a

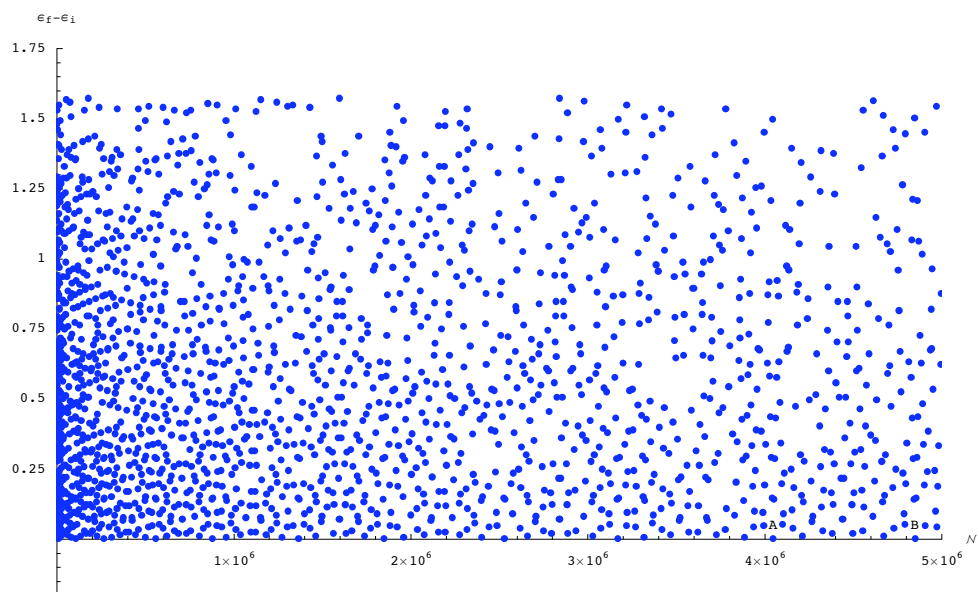


Figure 14b

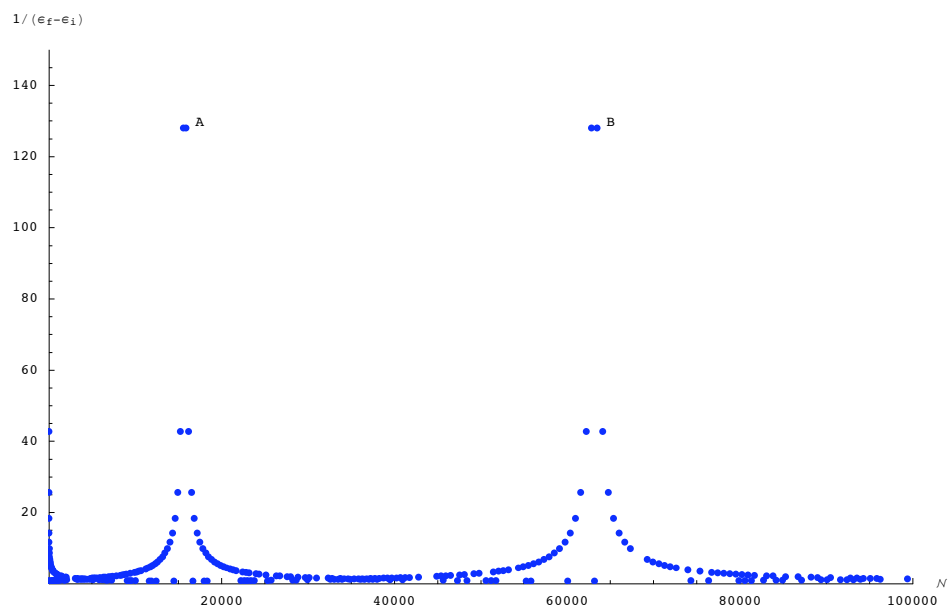


Figure 15a

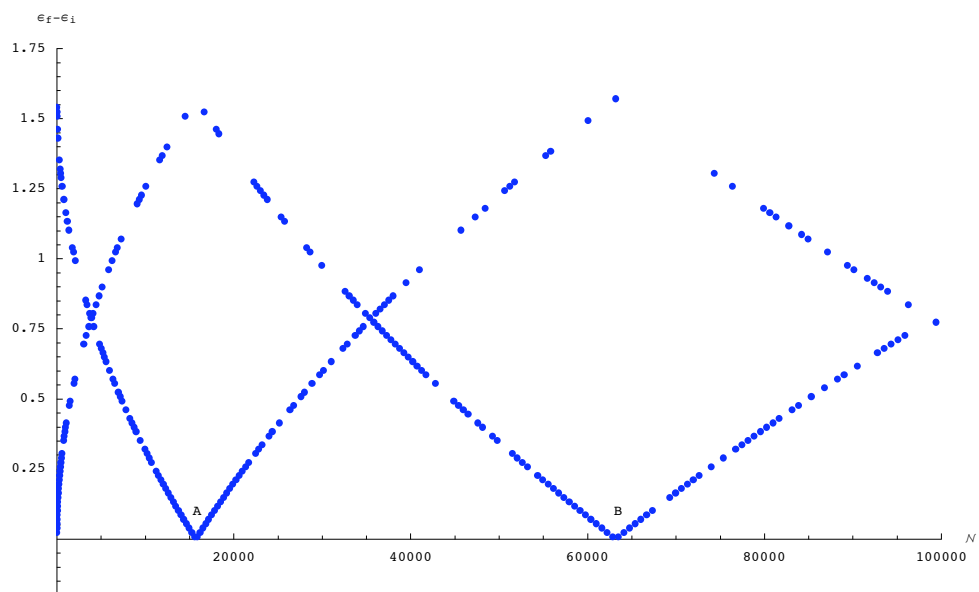


Figure 15b